Mechanistic insights on age-related changes in heart-aorta-brain hemodynamic coupling using a pulse wave model of the entire circulatory system

Arian Aghilinejad[1], Faisal Amlani[2], Sohrab P. Mazandarani[3], Kevin S. King[4], Niema M. Pahlevan[1, 5] *

[1] Department of Aerospace & Mechanical Engineering, University of Southern California, Los Angeles, USA
[2] Université Paris-Saclay, CentraleSupélec, ENS Paris-Saclay, CNRS, LMPS - Laboratoire de Mécanique Paris-Saclay, France
[3] Keck School of Medicine, Department of Medicine, University of Southern California, Los Angeles, USA
[4] Barrow Neurological Institute, Phoenix, USA
[5] Division of Cardiovascular Medicine, Department of Medicine, University of Southern California, Los Angeles, USA

*Correspondence: pahlevan@usc.edu

RUNNING TITLE: aging and heart-aorta-brain hemodynamics

Keywords: Aging, Vascular Dementia, Hemodynamics, Arterial Stiffening

ABSTRACT

Age-related changes in aortic biomechanics can impact the brain by reducing blood flow and increasing pulsatile energy transmission. Clinical studies have shown that impaired cardiac function in heart failure patients is associated with cognitive impairment. Although previous studies have attempted to elucidate the complex relationship between age-associated aortic stiffening and pulsatility transmission to the cerebral network, they have not adequately addressed the effect of interactions between aortic stiffness and left ventricle (LV) contractility (neither on energy transmission nor on brain perfusion). In this study, we utilize a well-established and validated one-dimensional blood flow and pulse wave computational model of the circulatory system in order to address how age-related changes in cardiac function and vasculature affect the underlying mechanisms involved in the LV-aorta-brain hemodynamic coupling. Our results reveal how LV contractility affects pulsatile energy transmission to the brain, even with preserved cardiac output. Our model demonstrates the existence of an optimal heart rate (near the normal human heart rate) that minimizes pulsatile energy transmission to the brain at different contractility levels. Our findings further suggest that the reduction in cerebral blood flow at low levels of LV contractility is more prominent in the setting of age-related aortic stiffening. Maintaining optimal blood flow to the brain requires either an increase in contractility or an increase in heart rate. The former consistently leads to higher pulsatile power transmission, and the latter can either increase or decrease subsequent pulsatile power transmission to the brain.

NEW AND NOTEWORTHY

We investigated the impact of major aging mechanisms of the arterial system and cardiac function on brain hemodynamics. Our findings suggest that aging has a significant impact on heart-aorta-brain coupling through changes in both arterial stiffening and left ventricle (LV) contractility. Understanding the underlying physical mechanisms involved here can potentially be a key step for developing more effective therapeutic strategies that can mitigate the contributions of abnormal LV-arterial coupling towards neurodegenerative diseases and dementia.

INTRODUCTION

The circulatory system operates based on a delicate hemodynamic balance between the heart, the aorta, and major target organs such as the brain (1, 2). In healthy young adults, interactions between the left ventricle (LV) and the aorta are optimized to guarantee the delivery of cardiac output (CO) with a modest pulsatile hemodynamic load on the LV (3, 4). In youth, the low impedance of a compliant aorta interacts with stiffer conduit arteries such as the carotid artery. This creates impedance mismatches and wave reflections at the aorta-brain boundaries that limit the transmission of excessive pulsatile energy into the cerebral microcirculation and protect the brain tissue (5, 6). It's worth noting that impedance mismatch is not the only theory explaining the brain's protective mechanism against excessive pulsatile energy transmission. As highlighted in other studies, factors such as vessel size and area should also be considered (7, 8). What is unquestionable, however, is that alteration in wave dynamics due to aortic stiffening leads to increased pulsatile energy transmission to the brain, which can be detrimental to the cerebral microvasculature and brain tissues (8). The optimum hemodynamic coupling between the LV, the aorta, and the brain can be impaired due to age-related changes in aortic stiffness (2, 9). Indeed, the stiffness increases with age and is one of the earliest pathological changes within the arterial wall, ultimately affecting the wave dynamics in the vasculature. This change can be identified before the onset of hypertension and may account for ethnic differences in cardiovascular and brain health (10-12). For heart-aorta coupling (LV-arterial coupling), previous studies have shown that elevated aortic stiffness increases the

LV pulsatile load, leading to an increase in LV mass which, in turn, contributes to the development of heart failure (HF) (13, 14). At the aorta-brain interface, it has been shown that disproportionate aortic stiffening increases aortic impedance, alters wave reflections, and increases the transmission of harmful pulsatile energy into the cerebrovascular network—ultimately leading to cognitive impairments such as Alzheimer's and other related vascular dementia (15, 16).

Furthermore, population-based clinical studies have suggested that HF patients with impaired LV function have worse degrees of cognitive impairment than age-matched individuals without HF (17, 18). HF has been proposed as a risk factor for Alzheimer's disease (AD), where the current clinical hypothesis is that the decreased cerebral blood flow due to HF may contribute to the dysfunction of the neurovascular unit and hence may lead to impaired clearance of amyloid beta (18-21). In addition to the consequences of HF, age-associated changes in ventricular wall thickening and stiffening may trigger heart remodeling that can also affect cerebral hemodynamics. Although previous studies have attempted to elucidate the complex relationship between aortic stiffness and pulsatile energy transmission to the brain (3, 6, 22), these studies have not adequately addressed the effect of interactions between the aorta and the LV on such energy transmission (nor on brain perfusion). Indeed, recent work has focused only on aorta-brain coupling and has not studied the impact of cardiac dynamics on cerebral perfusion (15). This may be due to the inherent difficulties in studying the isolated effects of aortic wave dynamics and cardiac function on brain hemodynamics in clinical settings (23, 24).

The state of LV-aorta-brain coupling is mainly dominated by: LV contractility (a major determinant of LV function), heart rate (a determinant of the fundamental frequency of propagated arterial waves), and aortic stiffness (a determinant of the buffering function of the aorta and pulse wave velocity). The optimal state of LV-aorta-brain coupling is achieved via the interplay of these three determinants (14, 22). The current study aims to gain mechanistic insight on age-related impacts to brain hemodynamics that are caused by alterations in the arterial system and cardiac function. In particular, we investigate the effects of LV contractility (as quantified by LV end-systolic elastance) and of aortic stiffness (as measured by pulse wave velocity, or PWV) on the transmission of pulsatile energy and flow to the brain. One-dimensional (1D) arterial pulse wave models (based on axisymmetric Navier-Stokes formulations) are well-established as physiologically-relevant tools to study global cardiovascular function (25-27). In this work, we such a modeling approach to the entire human circulation (28) using a high-order, FFT-based numerical methodology (29, 30)

METHODS

Physical Model of the Entire Human Circulation

A validated 1D model (28) of the complete circulatory system, based on space-time variables, was employed in this study. The physical model included 122 larger systemic arteries and 162 veins, each characterized by diameter, length, Young's modulus, and wall thickness. Fig. 1 illustrates the closed-loop cardiovascular model that consists of such 1D

63 segments for modeling wave propagation in larger arteries/veins, together with 0D
64 compartments for modeling all four heart chambers (including the left ventricle) as well as
65 the (truncated) microvasculature. The arterial wall is assumed to be thin, incompressible,
66 homogenous, and isotropic. In this study, we focused on investigating the effect of LV
67 dynamics and aortic stiffness on pulsatility transmission to the brain. Different levels of
68 aortic rigidity were considered by employing multiplicative factors of a minimum rigidity
69 level $E_1(x)$ that corresponds to the baseline PWV (c_0) that is initially prescribed in the
70 model. In order to simulate different states of LV contractility (30-33), the end-systolic
71 elastance (E_{es}) is varied. In this work, a value of E_{es}= 2.5 mmHg/mL is considered the
72 control and normotensive case, while values below 1.5 mmHg/mL and larger than 3.5
73 mmHg/mL are considered to be low and high contractility, respectively (34).

74 **Computational Model and Numerical Solver**

75 We adopt a nonlinear and physiologically-relevant fluid-structure model to simulate the
76 complete circulation, particularly the different material properties encountered in various
77 vascular segments (28, 35). For cross-sectional area $A = A(x,t)$ and mean velocity over
78 the cross-section $U = U(x,t)$ (yielding the flow rate as $Q = AU$), such a model can be
79 expressed as a reduced-order nonlinear system for each vessel segment by the expression

80 $$\begin{pmatrix} \frac{\partial A}{\partial \mathrm{t}}(x,t) \\ \frac{\partial U}{\partial t}(x,t) \end{pmatrix} = -\begin{pmatrix} \frac{\partial (AU)}{\partial x}(x,t) \\ U\frac{\partial U}{\partial x}(x,t)+\frac{1}{\rho}\frac{\partial P}{\partial x}(x,t)+\frac{2(\xi+2)\pi\mu U(x,t)}{\rho A(x,t)} \end{pmatrix} \quad (1)$$

81 where ρ is a (constant) blood density, μ is a (constant) blood viscosity, and ξ is a given
82 constant of an assumed axisymmetric velocity profile. The blood is assumed to be

Newtonian (36, 37). The system is closed by an assumed elastic (tube law) that accounts for the fluid-structure interaction and can be given by the constitutive law (38)

$$P = P_{\text{ext}} + \frac{\beta(x)}{A_{\text{d}}}\left(\sqrt{A} - \sqrt{A_{\text{d}}}\right),\ \beta(x) = \frac{4}{3}\sqrt{\pi}E(x)h(x) \tag{2}$$

where P_{ext} is the external and reference pressure, A_{d} is the diastolic area, and $\beta(x)$ is an expression of the arterial wall material properties in terms of elastic modulus $E(x)$ (a measure of stiffness) and wall thickness $h(x)$. To simulate multiple vessels, including vascular bifurcations or trifurcations, it is necessary to treat the fractal structure of the circulation network and, namely, branching points. These junctions effectively act as mathematical discontinuities in cross-sectional area and material properties. Physically, one must enforce continuity of total pressure and conservation of mass (flow rate) at junction points. For example, given a parent vessel p that splits into two daughter vessels $d_{\text{i}},\ \text{i} = 1,2$, the corresponding mathematical conditions are given by

$$P_p + \frac{\rho}{2}U_p = P_{d_{\text{i}}} + \frac{\rho}{2}U_{d_{\text{i}}},\ \text{i} = 1, 2, \tag{3}$$

$$\text{A}_p\text{U}_p + \text{A}_{d_1}\text{U}_{d_1} + \text{A}_{d_2}\text{U}_{d_2} = 0. \tag{4}$$

The overall numerical methodology for a vessel governed by Eqs. (1) and (2), together with the junction conditions of Eq. (3) and (4), is provided by a high-order Fourier continuation approach for hemodynamics equations introduced by Amlani and Pahlevan (30). Such a methodology enables long-time and long-distance wave propagation with minimal numerical dispersion or diffusion errors (29, 30, 39). A brief description of the

corresponding algorithm, as well as benchmark validation (38) of its implementation, is provided in the Appendix.

Following the works of Mynard and Smolich (28, 40), three types of vascular beds are considered: generic vascular beds (shown in Fig. 1), a hepatic vascular bed, and coronary vascular beds. The generic vascular bed model is used for all microvasculature beds except the liver and myocardium (28) and is based on the commonly used three-element Windkessel model. All baseline parameters of vessel segments and vascular beds are adopted from (28).

Time-varying Elastance Heart Model

The relationship between the pressure and the volume of a heart chamber is given by

$$P = P_{pc} + \frac{E_{\mathrm{nat}}}{E_{\mathrm{sep}}} P^{*} + E_{\mathrm{nat}}(V - V_{P=0}) - R_s q, \tag{5}$$

where P_{pc} is the pericardial pressure (assumed to depend exponentially on the total chamber volumes), E_{nat} is the native elastance of the chamber, E_{sep} is the septal elastance, $V_{P=0}$ is the volume of the chamber in zero pressure, R_{s} is the source resistance, and P^{*} is the pressure in the contralateral chamber. Parameters varied in this study and their corresponding range are listed in Table 1.

Hemodynamic Analysis

The total power $\bar{P}_{\mathrm{total}}$ transmitted to the brain over a cardiac cycle of length T is calculated as the average of the product of the pressure $P(t)$ and the flow $Q(t)$. We employ pressure

and flow data from the left common carotid artery for computing energy since it is the only cerebral branch directly connected to the aortic arch. The steady power $\bar{P}_{\mathrm{s}}$ is computed as the product of mean pressure P_{mean} and mean flow Q_{mean} in each segment. The pulsatile transmitted power $\bar{P}_{\mathrm{pulse}}$ is the difference between the total power and the steady power. Each of these power quantities is respectively given by

$$\bar{P}_{\mathrm{total}} = \frac{1}{T}\int_0^T P(t)Q(t)\mathrm{d}t, \tag{6}$$

$$\bar{P}_s = P_{\mathrm{mean}}Q_{\mathrm{mean}}, \tag{7}$$

$$\bar{P}_{\mathrm{pulse}} = \bar{P}_{\mathrm{total}} - \bar{P}_{\mathrm{s}}. \tag{8}$$

Total fluid flow transmitted to the cerebral network is computed by summing the average flow over one cardiac cycle (i.e., integrating over time) for all four arteries connected to the brain (two carotid and two vertebral). In addition to Eqs. (6)-(8), wave intensity (WI), a well-established clinical metric (41), is also considered in order to quantify energy transmission to the brain. Mathematically speaking, WI is computed as the product of the change in pressure ($\mathrm{d}P$) times the change in velocity ($\mathrm{d}U$) during a small interval, i.e.,

$$\mathrm{d}I = \mathrm{d}P.\mathrm{d}U. \tag{9}$$

To remove the dependency of $\mathrm{d}I$ on sampling time, the derivative of pressure and velocity are divided by the time interval (denoted as $\mathrm{d}P/\mathrm{d}t$ and $\mathrm{dU/dt}$, respectively), yielding units of power per unit area per unit time ($\mathrm{W.s^{-2}.m^{-2}}$) (41-43). To account for changes in the diameter, we also conducted wave power analysis (44). Wave power is defined as the

product of the pressure and volumetric flow signals and has the unit of the power (Watt) (45). We additionally investigated the reflection measures from wave separation analysis. To this end, the carotid pressure waveform is decomposed into its forward and backward components, following previous works (46, 47). The corresponding reflection index (RI, defined as the ratio of the peak backward pressure over the total pressure) is then computed and reported as a percentage.

As a third and final measure employed in this work, we also consider the Carotid (Flow) Pulsatility Index (CPI), a clinical parameter (2, 13) based on a single flow waveform measurement that is defined as

$$CPI = \frac{q_{\max} - q_{\min}}{\frac{1}{T}\int_0^T q(t)\mathrm{d}t}, \tag{10}$$

where $q_{\min}$ and $q_{\max}$ are, respectively, the minimum and maximum flow transmitted to the brain through the carotid artery during a cardiac cycle.

Fig 2 illustrates the impact of the elastance E_{es} on the LV pressure-volume loop. For example, varying E_{es}, while fixing the preload and LV end-diastolic volume (LVEDV), leads to different COs. In order to keep the CO constant at different levels of contractility, we adjust the LVEDV (Frank-Starling mechanism).

Statistical Analysis

We have conducted three ordinary least square regressions using a heteroscedasticity-consistent covariance matrix (HC3 type) (48) to assess the statistical significance of the relationship between the dependent variables (e.g., carotid pulsatile power) and the

corresponding independent variables. Independent variables in this study are considered to be LV contractility, aortic PWV, and heart rate. All independent variables have been incorporated in the models as categorical variables. The Shapiro-Wilk test for normality has been conducted in order to check the normality of each regression's residuals. The independence of the variables has also been tested by a Chi-Square test to check their correlations (no correlation has been found among the independent variables). Statistical significance is defined as $\alpha = 0.05/40 = 0.001$ (Bonferroni adjusted). The software package R version 4.2.2 has been used to conduct the statistical analysis.

RESULTS

Physiological Accuracy of the Model

Fig. 3 presents various pressure and flow waveforms, simulated via the numerical methodology described above, for cases of decreased ($E_{\mathrm{es}} = 1.2\,\mathrm{mHg/mL}$) and increased ($E_{\mathrm{es}} = 5.0\,\mathrm{mHg/mL}$) contractility, where LVEDV is adjusted to have the same CO for both ($5.60\,\mathrm{L/min}$). These cases are computed at a baseline heart rate (75 bpm) and aortic PWV ($4.66\,\mathrm{m/s}$), both within physiological ranges. The presented pressure and flow waveforms demonstrate the expected dynamics of the LV and the aorta during systole, including the presence of the pressure dicrotic notch as well as the physiological point-to-point consistency of the pressure with the flow. For the case of increased contractility, all waveforms have steeper upstrokes at the onset of ejection and reach their respective peaks earlier in systole. Even though varying LVEDV preserves CO, the peak flow is

significantly higher for the increased contractility case. Additionally, while pulse pressure minimally changes, the corresponding shape of the pressure waveform is affected by changes in contractility alone.

Fig. 3 further presents the computed carotid WI for the decreased and increased contractility cases. The curves fully capture the typical pattern of WI (41, 42, 49) a large-amplitude forward (positive) peak corresponding to the initial compression caused by LV contraction (Forward Compression Wave Intensity, or FCWI); a subsequent small-amplitude backward (negative) peak corresponding to the reflection of the initial contraction (Backward Compression Wave Intensity, BCWI); and a final moderate-amplitude forward decompression wave in protodiastole (Forward Expansion Wave Intensity, FEWI). The overall results of Fig. 3 demonstrate the general ability of our in-silico computational model to reproduce the physiological characteristics of the LV, the aorta, and the carotid artery.

Effect of LV Contractility on Transmitted Pulsatility to the Brain

Fig. 4, A presents the carotid pulsatile power (CPP) transmitted to the brain as a function of contractility for different levels of aortic PWV at a fixed LVEDV. The data is computed at the baseline heart rate (75 bpm). Since LVEDV is fixed, changes in contractility lead to corresponding changes in CO (see also Fig. 2), further compounding the overall effect of varying contractility by E_{es}. Fig. 4, B presents the isolated impact of contractility at a fixed CO (achieved by adjusting LVEDV) on the transmitted pulsatile power to the brain, where

200 it can be observed that, at all values of E_{es}, pulsatile power in the carotid artery increases
201 as a function of aortic PWV.

202 Fig. 5 presents CPP as a function of contractility (E_{es}) at different levels of both aortic
203 PWV and heart rate (*HR*). As before, to achieve a constant CO (5.6 L/min) at baseline
204 aortic PWV (c_0), values of LVEDV are accordingly adjusted; hence, at each PWV, the
205 changes in CPP are a consequence of the isolated changes in contractility. Results
206 demonstrate a trend towards increased transmitted pulsatile power to the brain as
207 contractility increases. However, the rate of this increase depends on HR. Table 2
208 additionally presents a comparison between baseline and increased aortic PWV (which can
209 result from aging) on CPP transmitted to the brain and further presents corresponding
210 values of the aortic pulsatility index (CPI) computed using Eq. (10).

Effect of Heart Rate on Transmitted Pulsatility to the Brain

Fig. 6 presents values of CPP as a function of HR for different levels of aortic PWV. The data in each plot is obtained at different levels of contractility (as measured by E_{es}). CO is fixed at each level of aortic PWV in a manner as has been described before. As HR increases, CPP decreases until the heart rate reaches an optimum point corresponding to where CPP is minimized. CPP increases with HR beyond this optimum point. Note that this phenomenon is present for all the different multiplicative factors of aortic PWV considered here, as well as for all the different levels of contractility. In all cases, the optimum point is located near the normal human heart rate (75 bpm). The p-values from a corresponding Shapiro-Wilk test are too large to reject the null hypothesis of the normality of the residuals. The coefficients of the regression results yield the expected signs and magnitudes. Additionally, by experimental design, our independent variables are uncorrelated; however, we have also conducted a Chi-Square test to check their correlations, and the results confirm the hypothesis (see Appendix for details). Indeed, the outcome of the statistical analysis reveals that an increase from the initial level of contractility (E_{es} = 0.6 mmHg/mL) to a contractility level of E_{es} = 1.2 mmHg/mL or E_{es} = 1.8 mmHg/mL is not statistically significant for CPP (see Appendix). On the other hand, the rest of the coefficients for other variables are significant, and all signs are found to be as expected. The impact of a change in HR is significant at all levels. Furthermore, CPP rises as the level of PWV rises, and all results are statistically significant (see Appendix).

231 Fig. 7 presents the carotid pulsatility index (CPI) as a function of HR for different levels
232 of aortic PWV. The data in each plot is obtained at different levels of contractility (as
233 measured by E_{es}). As before, CO is fixed at each level of aortic PWV. The results suggest
234 a trend toward increased CPI as HR increases. The statistical results (see Appendix) for
235 CPI demonstrate that CPI increases when independent variables increase; however, the
236 impact at the lower level of HR and contractility doesn't show statistical significance.

237 **Effect of LV-aorta Dynamics on Wave Intensity**

238 Fig. 8 presents calculated carotid WI patterns from simulations at different levels of aortic
239 PWV for different HR and contractility values. Similarly to Fig. 3, these patterns capture
240 all the well-known fiducial features (41), including the large-amplitude forward (positive)
241 peak FCWI that is followed in sequence by both a small-amplitude backward (negative)
242 peak BCWI and a moderate-amplitude forward decompression wave FEWI. Sample
243 patterns of aortic wave intensity at different levels of contractility are presented in the
244 Appendix (Fig. A3).

245 Table 3 presents peak amplitudes of the major features of WI (FCWI, BCWI, and FEWI)
246 at different levels of contractility. The data are presented at normal HR for both baseline
247 aortic PWV and an increased PWV. For reference, we have also included the amplitude of
248 the first peak of the wave power (forward compression wave power; FCWP) in Table 3.
249 The reflection index (as a percentage) at different contractility values, determined from
250 carotid pressure wave separation, is also reported in Table 3.

Table 4 presents peak amplitudes of the major features of WI (FCWI, BCWI, and FEWI) at different HR. The data are presented for both baseline aortic PWV and an increased PWV at a state of normal contractility (E_{es} = 2.5 mmHg/mL). Similarly to Table 3, we have also included the amplitude of the first peak of the wave power (FCWP) in Table 4. The reflection index for the carotid pressure at different values of heart rate is also reported Table 4.

Effect of LV-aorta Dynamics on Brain Perfusion

Fig. 9 demonstrates how changes in aortic stiffness (as measured by PWV) at different levels of contractility affect transmitted cerebral blood flow (CBF). The data in each plot is obtained at different heart rates. At each wave state, the percentage change is computed by the change in flow relative to baseline PWV. Note that at each contractility, LVEDV remains fixed. Results suggest a trend towards decreased cerebral flow as aortic stiffness increases. The rate of this change depends on the contractility and HR. The regression results (see Appendix) indicate that CBF decreases monotonically as the level of PWV increases, where the coefficients are statistically significant.

DISCUSSION

In this study, we have investigated the effect of LV-aortic dynamics on brain perfusion and the transmission of excessive wave pulsatility to cerebral circulation. We have modeled age-related changes in the arterial system and cardiac dynamics. Our results suggest that: (1) LV contractility by itself affects the pulsatile energy transmission to the brain (even at a preserved cardiac output); (2) at different levels of LV contractility and aortic stiffness, there exists an optimum wave condition, occurring near the normal human heart rate (75bpm), in which excessive pulsatile energy (power) transmission to the brain is minimized; and (3) at a given heart rate and LV contractility, greater aortic stiffness leads to lower cerebral blood flow. At the limit of brain autoregulation, the compensatory mechanism for adjusting the cerebral flow is achieved either by increasing the LV

277 contractility or the heart rate. Our results suggest that the former consistently leads to
278 higher pulsatile power transmission. The latter can either increase (for values less than
279 normal heart rate) or decrease (for values beyond normal heart rate) pulsatile power
280 transmission to the brain.

281 **Impact of LV Contractility**

282 We have utilized a reduced-order 1D model of the entire human circulation to study and
283 elucidate the underlying mechanisms involved in LV-aorta-brain hemodynamic coupling.
284 The numerical solver employed in this work incorporates the nonlinear and nonstationary
285 coupling of various cardiovascular system components (including an ODE-based four-
286 chamber heart model with valves), where the validation results that have been presented
287 support its suitability for the objectives of this study. Results further demonstrate that our
288 model can adequately capture the effects of contractility on central and peripheral pressure
289 waveforms (Fig. 3). The expectedly steeper upstrokes in both pressure and aortic flow
290 waveforms for increased contractility are well-captured in this model and are consistent
291 with previous studies (23). Our findings suggest that increased LV contractility alone can
292 directly alter central and peripheral hemodynamics, even for unchanged arterial loads and
293 cardiac outputs. These observations are consistent with previous experimental and clinical
294 studies (14, 50).

295 The first principal finding in this study is related to examining the impact of LV
296 contractility on transmitted energy and pulsatility to the cerebral network, where we have
297 used end-systolic elastance (E_{es}) as a measure to quantify the state of LV contractility. Fig.

4 demonstrates the true effect of contractility on pulsatile energy transmission to the brain (where CO is fixed by adjusting LVEDV; see Fig. 2), where our results suggest that even at a fixed CO, an increase in contractility alone can lead to elevated levels of harmful pulsatile energy transmission to the brain. This behavior is also a function of aortic stiffness (Fig. 4). However, the rate of increase in pulsatile energy transmission as a function of contractility is slower when the CO is compensated for than when the CO is affected by changes in E_{es}. In other words, the impact of contractility on the cerebral pulsatile power depends on the preload (measured by LVEDV) as well. As preload is adjusted to compensate CO, the effect of contractility is less pronounced. Since CO and the total arterial resistance of the system is the same for different levels of contractility (at the same aortic PWV), the steady portion of the transmitted power does not change (14). However, since the shape of the pressure also changes due to contractility, the total power increases (Eq. (6)), leading to an increase in the transmitted pulsatile power (Eq. (8)).

Results also suggest that the impact of contractility on brain perfusion depends on heart rate (Fig. 5 and Table 2). At lower heart rates, changes in carotid pulsatile power are more pronounced than at higher heart rates. At a fixed travel time (keeping PWV constant), changing the heart rate affects the interaction between the compression waves generated by the LV and the reflected waves due to vessel branching (31, 51). The sample net effect of these two types of waves is illustrated in the WI patterns of Fig. 3 and Fig. 8. These interactions become less sensitive to contractility at higher heart rates. Hence, the pulsatile portion of the power varies less. This pattern can be observed at all levels of aortic stiffness

considered in this work. Another major finding in this study is the relation between volume blood flow transmission to the brain and heart contractility, as shown in Fig. 9. Results suggest that decreased contractility at fixed heart rate and aortic PWV leads to a reduction in volume blood flow transmission (brain malperfusion). This can explain one of the underlying mechanisms involved in heart failure-induced brain injury (where LV contractility is impaired).

Presence of an Optimum Heart Rate

Our results indicate there is an optimum heart rate at which the transmitted carotid pulsatile energy is minimized (Fig. 6). This is consistent with previous findings (22). Pulsatile energy decreases with increasing heart rate until it reaches this minimum value. Beyond this value, waves transmitted to the brain begin to act destructively, and, as a result, pulsatile power starts increasing as the heart rate increases. This has implications for the aging population, where resting HR generally increases (52, 53). Additionally, aging leads to the stiffening of the aorta, further increasing the pulsatile energy transmission to the brain. Indeed, our findings are consistent with previous studies (2, 51) suggesting that aortic wave optimization is one of the key design characteristics in the mammalian cardiovascular system. To the best of our knowledge, the presence of the optimum heart rate at different levels of contractility in the LV-aorta-brain system has not been reported in prior studies (including from in-vivo experiments).

In contrast to pulsatile energy, which requires both flow and pressure waveforms to calculate, the carotid flow pulsatility index (CPI) is a conventional dimensionless

parameter quantifying hemodynamic pulsatility transmission to cerebrovasculature based only on flow measurements (2, 13). Fig. 7 presents CPI values corresponding to the same values of heart rate, contractility, and aortic PWV considered for our pulsatile energy analysis. A trend of increasing CPI with increasing heart rate can be observed in all cases. However, the CPI curves do not capture the non-linearity and the presence of a minimum that can be found in the CPP curves of Fig. 6. A statistical analysis of the coefficients reveals that the impact of lower levels of heart rate is statistically significant on CPI, although this impact doesn't show statistical significance on the CPI results (Table A2 and A3 in Appendix). This suggests that considering the flow waveform alone may not be adequate in properly quantifying the pulsatility transmitted to the brain and that consideration of energy-based methods that include both pressure and flow; hence we suggest that future clinical studies should include both indices in their assessments. This is particularly prudent since aortic aging simultaneously affects the transmitted flow and pressure waves to the brain (22).

Impact of Aortic Stiffness (Vascular Aging)

Aortic stiffening is the primary cause of systolic hypertension with aging (54). It has been shown that blood pressure lowering with antihypertensive agents compared with control is significantly associated with a lower risk of incident dementia or cognitive impairment (55). In prior work, we have shown such age-related stiffening (22, 56) is a powerful predictor of insult to the microvasculature in the brain, more so than blood pressure (16). Our results in this work confirm that aortic stiffening does indeed increase the transmission

of harmful pulsatility to the brain. This excessive pulsatility can be observed at all contractility states in both CPP (Fig. 6) and CPI (Fig. 7). For example, age-related changes in aortic biomechanics can lead to an increase from the average aortic PWV of 7 m/s for a young adult to an average aortic PWV of 14 m/s for an old individual (57). This age-related increase in aortic PWV under normal contractility leads to a 42% increase in pulsatile energy transmission to the brain. The effect of these age-related changes becomes even more pronounced when compounded with increased contractility. For example, changes in aortic PWV and contractility from normal values for a young adult to increased values for an old individual can elevate the pulsatile energy transmission to the brain more than 200%.

Results from Fig. 9 further suggest that greater aortic stiffness leads to lower cerebral blood flow at a fixed heart condition (i.e., a fixed contractility). A statistical analysis confirms a significant dependency for cerebral blood flow on aortic stiffness (Table A4 in Appendix). These findings are consistent with a recent population-based clinical study by Jefferson, et al. (58), where it was reported that more significant aortic stiffening relates to lower cerebral blood flow, especially among individuals with an increased genetic predisposition for Alzheimer's disease. The authors have hypothesized that this mechanism is due to microcirculatory remodeling in response to higher pulsatility in the cerebrovascular network. In our present investigation, an isolated increase in aortic stiffness (under fixed contractility) leads to decreased blood flow transmission to the brain (58). Therefore, the effects of harmful carotid pulsatile energy transmission are likely compounded with the decreased flow transmission to the brain as a result of such age-related aortic stiffening.

A decreased cerebral blood flow, which can result from systemic diseases such as heart failure, can contribute to the dysfunction of the neurovascular unit (18). This is the prevailing view of the underlying mechanism of HF-induced Alzheimer's disease (17). Our results suggest that at low levels of LV contractility, the reduction in cerebral blood flow due to age-related changes in aortic stiffness becomes even more pronounced (Fig. 9). To counteract this suboptimal flow, the brain may employ its autoregulatory mechanism by reducing the resistance. However, this effort to maintain perfusion may have other deleterious effects, such as allowing further penetration of pulsatile energy into the microvasculature where it may cause more damage (8). Additionally, the autoregulatory capacity of the brain may be limited in the setting of microvascular disease (8, 10, 12). Under these circumstances, the body needs to either increase the heart rate or the contractility in order to compensate for and to regulate the blood flow to the brain. The latter leads to higher harmful pulsatile energy transmission to the brain (Figs. 4 and 5). On the other hand, increasing the heart rate can both decrease or increase this energy transmission (Fig. 6), depending on whether the increasing HR is approaching or diverging from the minimum, respectively. Since the resting heart rate in the elderly is usually higher than the normal human heart rate (i.e., the latter case), an increase in pulsatile energy transmission will be observed (which, as explained before, can have detrimental effects on brain structure). Overall, our results demonstrate that age-relating aortic stiffening can lead to a cascade of detrimental effects, due to changes in contractility and HR, on both cerebral perfusion and pulsatile energy transmission to the brain. Fig. 10 summarizes this

compensatory mechanism for cerebral blood flow in the context of heart-aorta-brain coupling based on the findings of this study.

Pulse Wave Analysis

Wave intensity (WI) analysis is a well-established method for quantifying the energy carried in arterial waves (49, 59-61). In a recent population-based clinical study, Chiesa et al. (62) showed that elevated carotid WI, captured in FCWI amplitudes (e.g., in Fig. 3), predicts faster cognitive decline in long-term follow-ups independently of other cardiovascular risk factors. Their findings suggest that exposure to increased WI in mid- to late-life may contribute to the observed association between arterial stiffness in mid-life and the risk of dementia in the following decades. This cannot be detected using common carotid phenotypes (62). Our results are consistent with such observations, where one can observe that elevated aortic stiffness leads to higher WI (Fig. 8 and Table 4). Our results also demonstrate that elevated FCWI not only depends on aortic stiffness but also strongly upon LV contractility (Fig. 8 and Table 3). This can be mainly attributed to the larger dP/dt resulting from increased contractility, which manifests as sharper pressure slopes in early systole and more pronounced forward compression waves (Tables 3 and 4). Similar trends can also be observed in FCWP amplitudes. The difference between wave intensity and wave power is rooted in their definition; the latter is not sensitive to variations in cross-sectional area, and thus, it is conserved at junctions (44, 45). Our results suggest that these patients might also suffer from excessive FCWI and FCWP, which could have adverse effects on brain structure (1-3, 16, 62). Tables 3 and 4 also present results for the computed

reflection index at different contractility values and at different levels of the heart rate. Our results indicate that elevated aortic stiffness leads to an increase in the reflection index (Tables 3 and 4). Results also suggest that reflection index is higher at lower heart rates (below 75bpm) and increased contractility (above 2.5 mmHg/mL). Both these conditions may have adverse effects on cerebral circulation, particularly in terms of pulsatile energy transmission to the brain (Figures 5 and 6.

Limitations

The primary limitation of this study is in the vessel wall assumptions of the 1D vasculature model formulation, i.e., neglecting the viscoelasticity (which may be important to consider in certain vessels (60, 63)). However, our model still employs an effective nonlinear/hyperelastic wall model that has been shown previously to be appropriate under normal physiological conditions and does not lead to considerable differences with viscoelastic considerations (35). In addition, we have not included any autoregulatory models for brain circulation. However, since this study aims to investigate the impact of LV-aorta dynamics on general brain hemodynamics, the feedback response of the brain on such dynamics is beyond the scope of this work. Lastly, while we examined a large range of the heart rates in our study (from 30bpm to 180bpm), the mechanistic model that we propose here is based on a stable heart rate. Future work can focus on the impact of irregular heart rate that can happen under certain cardiovascular conditions such as atrial fibrillation.

CONCLUSION

We have demonstrated that alterations in LV contractility can affect pulsatile energy transmission to the brain. We have additionally demonstrated an optimum wave condition, existing at different levels of contractility, heart rate, and aortic stiffness, that minimizes this harmful pulsatile energy. We have shown that this optimum condition occurs near the normal human heart rate and remains constant across a wide range of aortic arch stiffnesses and LV contractility. Our findings also suggest that greater aortic stiffness leads to higher pulsatile energy transmission to the brain and to lower cerebral volume blood flow. These principal findings not only demonstrate the level of coupling in the LV-aorta-brain system but also demonstrate how such coupling is affected by age-related changes to the cardiovascular system. Understanding the underlying physical mechanisms involved is an important step toward developing improved therapeutic strategies for vascular-related neurodegenerative diseases. All in all, the insight from our work is central to answering questions about proper management of blood pressure and aortic stiffness among the elderly. Our results suggest that the age-related changes in aortic stiffness and contractility both affect the cerebral blood flow. Hence, it is crucial to consider the impact of antihypertensive treatment on these age-related factors and the resulting impact on cerebral blood flow. Ultimately, our findings suggest that more rational and individualized antihypertensive therapy (e.g., not only based on systolic pressure level) is needed to preclude such cerebrovascular events.

APPENDIX

The numerical model

The numerical methodology for solving the partial differential equation (PDE) system of Eqs. (1)-(2) is based on a Fourier continuation (FC) approach that has been introduced previously for 1D arterial wave propagation [JCP 2020]. Both implicit and explicit FC-based PDE solvers have been successfully constructed and utilized for a variety of physical problems, including those governed by advection-diffusion equations**,** Navier-Cauchy elastodynamics equations, Navier-Stokes fluid equations, and fluid-structure equations (29, 30, 39, 64, 65).

Validations of the complete numerical solver have been conducted using the benchmark problems proposed in (38). Fig. A1 presents pressure and flow solutions of a single-segment common carotid artery (with Windkessel) benchmark using both FC as well as commonly used discontinuous Galerkin (DCG) (38) and locally conservative Galerkin (LCG) methods (66). Figs. A2 additionally presents corresponding FC, DCG and LCG simulated pressure and flow at midpoints of various vascular segments from a benchmark problem (38) on a 77-segment open-loop model (that considers 56 major arteries). Parameters for these benchmarks can be found in the respective source (38). For both problems, Figs. A1 and A2 demonstrate excellent correspondence between the solutions generated by the FC solver employed in this work and those generated by other numerical schemes.

Aortic wave intensity pattern

Fig. A3 presents calculated aortic WI patterns from simulations at different contractility values. These patterns are presented for the normal heart rate (75bpm) and the baseline aortic stiffness. Results indicate a distinct midsystolic forward traveling front (which is a function of contractility) in both carotid and aortic WI patterns, with it being more pronounced in the carotid, as demonstrated in Fig. 8."

Statistical analysis

The summary of the Shapiro-Wilk test to check the normality of each regression's residuals is presented in Table A1.

The regression model outcomes for three dependent variables, CPI, CPP, and CBF, are presented in Tables A2, A3, and A4, respectively. Independent variables in this study are LV contractility, aortic PWV, and heart rate. All independent variables are incorporated in the models as categorical variables. The minimum baseline for the heart rate is 30 bpm, for the contractility is 0.6 mmHg/mL, and for the aortic PWV is c_0.

ACKNOWLEDGEMENT

Arian Aghilinejad is the recipient of an American Heart Association Predoctoral fellowship. Niema Pahlevan acknowledges support from the National Science Foundation (NSF CAREER Award Number 2145890). This study was partially funded by the National Institutes of Health (NIH; No. 1R56AG068630-01).

DISCLOSURE

The authors report no conflict of interest.

FIGURE LEGENDS

Figure 1 Closed-loop cardiovascular model consisting of 1D segments coupled to 0D lumped-parameter models of the heart and microvasculature.

Figure 2 A) Schematic representation of the human circulatory system; B) interventricular pressure-volume loops for different cases of contractility (demarcated in different line styles and colors); and C) the compounded impact (a fixed LVEDV) and the isolated impact (a fixed CO) of contractility.

Figure 3 Effects of LV contractility on *aortic and carotid* hemodynamics. *CO* is the same for both sets of figures on the right and left panels. The figures on the left panel demonstrate the impact of reduced contractility, and the figures on the right panel demonstrate the impact of increased contractility. FCWI: Forward Compression Wave Intensity; BCWI: Backward Compression Wave Intensity; FEWI: Forward Expansion Wave Intensity.

Figure 4 Carotid pulsatile power (CPP) per cardiac cycle versus contractility (as measured by E_{es}) at different levels of aortic stiffness at (A) fixed LVEDV (changing CO) and (B) fixed CO.

Figure 5 Carotid pulsatile power (CPP) per cardiac cycle versus contractility (as measured by E_{es}) at different levels of aortic stiffness at other heart rates: (A) HR=30 bpm, (B) HR=50 bpm, (C) HR=100 bpm, and (D) HR=125 bpm.

Figure 6 Carotid pulsatile power (CPP) per cardiac cycle versus HR at different levels of aortic stiffness: (A) E_{es} of 0.6 mmHg/mL, (B) E_{es} of 1.2 mmHg/mL, (C) E_{es} of 1.8 mmHg/mL, (D) E_{es} of 2.5 mmHg/mL, (E) E_{es} of 3.5 mmHg/mL, and (F) E_{es} of 5.0 mmHg/mL.

Figure 7 Carotid pulsatility index (CPI) per cardiac cycle versus HR at different levels of aortic stiffness: (A) E_{es} of 0.6 mmHg/mL, (B) E_{es} of 1.2 mmHg/mL, (C) E_{es} of 1.8 mmHg/mL, (D) E_{es} of 2.5 mmHg/mL, (E) E_{es} of 3.5 mmHg/mL, and (F) E_{es} of 5.0 mmHg/mL.

Figure 8 Sample carotid Wave Intensity (WI) patterns at different HR and different levels of contractility (as measured by E_{es}). Each plot contains data obtained at different levels of aortic stiffness (quantified by PWV).

Figure 9 Change in the transmitted flow to the brain versus aortic stiffness (as measured by PWV) at different levels of contractility: (A) HR=30 bpm, (B) HR=75 bpm, (C) HR=125 bpm, and (D) HR=180 bpm.

Figure 10 Mechanistic model, based on the findings of this study, for compensating cerebral blood flow due to pathological aging.

Figure A1 Single segment benchmark. Pressure (left) and flow rate (right) at the midpoint of the common carotid artery (CCA) simulated by Fourier continuation (FC; the solver used in this work), discontinuous Galerkin (DCG) (38), and locally conservative Galerkin (LCG) (66) methods. Lines are plotted at a resolution of $\Delta t = 10^{-3}s$, and markers are plotted every 10 such timesteps ($10^{-2}\,s$) for easier visualization. *Provided by the supplementary data files in (38).

Figure A2 77-segment (ADAN56) benchmark. Pressure (left) and flow rate (right) at the midpoint of (from top row to bottom) the aortic arch (AorticArchI), abdominal aorta (AbdomAortaV), and right common carotid artery (RightCCA) simulated by Fourier continuation (FC), discontinuous Galerkin (DCG) (38), and locally conservative Galerkin (LCG) (66) methods. Lines are plotted at a resolution of $\Delta t = 10^{-3}s$, and markers are plotted every 10 such timesteps ($10^{-2}\,s$) for easier visualization. *Provided by the supplementary data files in (38).

Figure A3 Sample aortic Wave Intensity (WI) patterns at different levels of contractility (as measured by E_{es}).

REFERENCES

1. **Maroules CD, Khera A, Ayers C, Goel A, Peshock RM, Abbara S, and King KS**. Cardiovascular outcome associations among cardiovascular magnetic resonance measures of arterial stiffness: the Dallas heart study. *Journal of Cardiovascular Magnetic Resonance* 16: 33, 2014.
2. **Mitchell GF, van Buchem MA, Sigurdsson S, Gotal JD, Jonsdottir MK, Kjartansson Ó, Garcia M, Aspelund T, Harris TB, and Gudnason V**. Arterial stiffness, pressure and flow pulsatility and brain structure and function: the Age, Gene/Environment Susceptibility–Reykjavik study. *Brain* 134: 3398-3407, 2011.
3. **Mitchell GF**. Effects of central arterial aging on the structure and function of the peripheral vasculature: implications for end-organ damage. *Journal of applied physiology* 105: 1652-1660, 2008.
4. **Bell V, and Mitchell GF**. Influence of vascular function and pulsatile hemodynamics on cardiac function. *Current hypertension reports* 17: 1-9, 2015.
5. **de Roos A, van der Grond J, Mitchell G, and Westenberg J**. Magnetic resonance imaging of cardiovascular function and the brain: is dementia a cardiovascular-driven disease? *Circulation* 135: 2178-2195, 2017.
6. **Stone J, Johnstone DM, Mitrofanis J, and O'Rourke M**. The mechanical cause of age-related dementia (Alzheimer's disease): the brain is destroyed by the pulse. *Journal of Alzheimer's Disease* 44: 355-373, 2015.
7. **Chirinos JA**. Large artery stiffness, microvascular function, and cardiovascular risk. Am Heart Assoc, 2016, p. e005903.
8. **Chirinos JA, Segers P, Hughes T, and Townsend R**. Large-artery stiffness in health and disease: JACC state-of-the-art review. *Journal of the American College of Cardiology* 74: 1237-1263, 2019.
9. **Maillard P, Mitchell GF, Himali JJ, Beiser A, Tsao CW, Pase MP, Satizabal CL, Vasan RS, Seshadri S, and DeCarli C**. Effects of arterial stiffness on brain integrity in young adults from the Framingham Heart Study. *Stroke* 47: 1030-1036, 2016.
10. **King KS, Sheng M, Liu P, Maroules CD, Rubin CD, Peshock RM, McColl RW, and Lu H**. Detrimental effect of systemic vascular risk factors on brain hemodynamic function assessed with MRI. *The neuroradiology journal* 31: 253-261, 2018.
11. **Goel A, Maroules CD, Mitchell GF, Peshock R, Ayers C, McColl R, Vongpatanasin W, and King KS**. Ethnic difference in proximal aortic stiffness: an observation from the Dallas Heart Study. *JACC: Cardiovascular Imaging* 10: 54-61, 2017.
12. **Maroules CD, Khera A, Ayers C, Goel A, Peshock RM, Abbara S, and King KS**. Cardiovascular outcome associations among cardiovascular magnetic resonance measures of arterial stiffness: the Dallas heart study. *Journal of Cardiovascular Magnetic Resonance* 16: 1-9, 2014.
13. **Mitchell GF, Tardif J-C, Arnold JMO, Marchiori G, O'Brien TX, Dunlap ME, and Pfeffer MA**. Pulsatile hemodynamics in congestive heart failure. *Hypertension* 38: 1433-1439, 2001.
14. **Pahlevan NM, and Gharib M**. Aortic wave dynamics and its influence on left ventricular workload. *PloS one* 6: e23106, 2011.
15. **van Sloten TT, Protogerou AD, Henry RM, Schram MT, Launer LJ, and Stehouwer CD**. Association between arterial stiffness, cerebral small vessel disease and cognitive impairment: a systematic review and meta-analysis. *Neuroscience & Biobehavioral Reviews* 53: 121-130, 2015.
16. **King KS, Chen KX, Hulsey KM, McColl RW, Weiner MF, Nakonezny PA, and Peshock RM**. White matter hyperintensities: use of aortic arch pulse wave velocity to predict volume independent of other cardiovascular risk factors. *Radiology* 267: 709-717, 2013.

17. **Havakuk O, King KS, Grazette L, Yoon AJ, Fong M, Bregman N, Elkayam U, and Kloner RA**. Heart failure-induced brain injury. *Journal of the American College of Cardiology* 69: 1609-1616, 2017.
18. **Cermakova P, Eriksdotter M, Lund L, Winblad B, Religa P, and Religa D**. Heart failure and Alzheimer′ s disease. *Journal of internal medicine* 277: 406-425, 2015.
19. **Rajagopalan B, Raine AE, Cooper R, and Ledingham JG**. Changes in cerebral blood flow in patients with severe congestive cardiac failure before and after captopril treatment. *The American journal of medicine* 76: 86-90, 1984.
20. **Cohn JN, Levine TB, Olivari MT, Garberg V, Lura D, Francis GS, Simon AB, and Rector T**. Plasma norepinephrine as a guide to prognosis in patients with chronic congestive heart failure. *New England journal of medicine* 311: 819-823, 1984.
21. **Chhatre S, Weiner MG, Jayadevappa R, and Johnson JC**. Incremental burden of congestive heart failure among elderly with Alzheimer's. *Aging & mental health* 13: 628-634, 2009.
22. **Aghilinejad A, Amlani F, King KS, and Pahlevan NM**. Dynamic effects of aortic arch stiffening on pulsatile energy transmission to cerebral vasculature as a determinant of brain-heart coupling. *Scientific reports* 10: 1-12, 2020.
23. **Pagoulatou S, Adamopoulos D, Rovas G, Bikia V, and Stergiopulos N**. The effect of left ventricular contractility on arterial hemodynamics: A model-based investigation. *PloS one* 16: e0255561, 2021.
24. **Gaddum N, Alastruey J, Chowienczyk P, Rutten MC, Segers P, and Schaeffter T**. Relative contributions from the ventricle and arterial tree to arterial pressure and its amplification: an experimental study. *American Journal of Physiology-Heart and Circulatory Physiology* 313: H558-H567, 2017.
25. **Sherwin SJ, Franke V, Peiro J, and Parker K**. One-dimensional modelling of a vascular network in space-time variables. *J Eng Math* 47: 217-250, 2003.
26. **Pan Q, Wang R, Reglin B, Fang L, Yan J, Cai G, Kuebler WM, Pries AR, and Ning G**. Pulse wave velocity in the microcirculation reflects both vascular compliance and resistance: Insights from computational approaches. *Microcirculation* 25: e12458, 2018.
27. **Alastruey J, Charlton PH, Bikia V, Paliakaitė B, Hametner B, Bruno RM, Mulder MP, Vennin S, Piskin S, and Khir AW**. Arterial pulse wave modelling and analysis for vascular age studies: a review from VascAgeNet. *American Journal of Physiology-Heart and Circulatory Physiology* 2023.
28. **Mynard JP, and Smolich JJ**. One-dimensional haemodynamic modeling and wave dynamics in the entire adult circulation. *Annals of biomedical engineering* 43: 1443-1460, 2015.
29. **Amlani F, and Bruno OP**. An FC-based spectral solver for elastodynamic problems in general three-dimensional domains. *Journal of Computational Physics* 307: 333-354, 2016.
30. **Amlani F, and Pahlevan NM**. A stable high-order FC-based methodology for hemodynamic wave propagation. *Journal of Computational Physics* 405: 109130, 2020.
31. **Aghilinejad A, Wei H, Magee GA, and Pahlevan NM**. Model-Based Fluid-Structure Interaction Approach for Evaluation of Thoracic Endovascular Aortic Repair Endograft Length in Type B Aortic Dissection. *Frontiers in Bioengineering and Biotechnology* 10: 2022.
32. **Berger DS, Li J, and Noordergraaf A**. Differential effects of wave reflections and peripheral resistance on aortic blood pressure: a model-based study. *American Journal of Physiology-Heart and Circulatory Physiology* 266: H1626-H1642, 1994.
33. **Aghilinejad A, Wei H, Bilgi C, Paredes A, DiBartolomeo A, Magee GA, and Pahlevan NM**. Framework Development for Patient-Specific Compliant Aortic Dissection Phantom Model Fabrication: Magnetic Resonance Imaging Validation and Deep-Learning Segmentation. *Journal of Biomechanical Engineering* 145: 091010, 2023.
34. **Kawaguchi M, Hay I, Fetics B, and Kass DA**. Combined ventricular systolic and arterial stiffening in patients with heart failure and preserved ejection fraction: implications for systolic and diastolic reserve limitations. *Circulation* 107: 714-720, 2003.

35. **Huttunen JM, Kärkkäinen L, and Lindholm H**. Pulse transit time estimation of aortic pulse wave velocity and blood pressure using machine learning and simulated training data. *PLoS computational biology* 15: e1007259, 2019.
36. **Aghaamoo M, Aghilinejad A, Chen X, and Xu J**. On the design of deterministic dielectrophoresis for continuous separation of circulating tumor cells from peripheral blood cells. *Electrophoresis* 40: 1486-1493, 2019.
37. **Aghilinejad A, Aghaamoo M, and Chen X**. On the transport of particles/cells in high-throughput deterministic lateral displacement devices: Implications for circulating tumor cell separation. *Biomicrofluidics* 13: 2019.
38. **Boileau E, Nithiarasu P, Blanco PJ, Müller LO, Fossan FE, Hellevik LR, Donders WP, Huberts W, Willemet M, and Alastruey J**. A benchmark study of numerical schemes for one-dimensional arterial blood flow modelling. *International journal for numerical methods in biomedical engineering* 31: e02732, 2015.
39. **Amlani F, Bhat HS, Simons WJ, Schubnel A, Vigny C, Rosakis AJ, Efendi J, Elbanna AE, Dubernet P, and Abidin HZ**. Supershear shock front contribution to the tsunami from the 2018 M w 7.5 Palu, Indonesia earthquake. *Geophysical Journal International* 230: 2089-2097, 2022.
40. **Mynard JP, and Smolich JJ**. Influence of anatomical dominance and hypertension on coronary conduit arterial and microcirculatory flow patterns: a multiscale modeling study. *American Journal of Physiology-Heart and Circulatory Physiology* 311: H11-H23, 2016.
41. **Parker KH**. An introduction to wave intensity analysis. *Medical & biological engineering & computing* 47: 175, 2009.
42. **Parker KH, and Jones C**. Forward and backward running waves in the arteries: analysis using the method of characteristics. 1990.
43. **Smolich JJ, Mynard JP, and Penny DJ**. Wave intensity analysis of right ventricular and pulmonary vascular contributions to higher pulmonary than aortic blood pressure in fetal lambs. *American Journal of Physiology-Heart and Circulatory Physiology* 299: H890-H897, 2010.
44. **Mynard JP, and Smolich JJ**. Novel wave power analysis linking pressure-flow waves, wave potential, and the forward and backward components of hydraulic power. *American Journal of Physiology-Heart and Circulatory Physiology* 310: H1026-H1038, 2016.
45. **Mynard JP, Kondiboyina A, Kowalski R, Cheung MM, and Smolich JJ**. Measurement, analysis and interpretation of pressure/flow waves in blood vessels. *Frontiers in Physiology* 11: 1085, 2020.
46. **Manisty C, Mayet J, Tapp RJ, Parker KH, Sever P, Poulter NH, Thom SAM, Hughes AD, and Investigators A**. Wave reflection predicts cardiovascular events in hypertensive individuals independent of blood pressure and other cardiovascular risk factors: an ASCOT (Anglo-Scandinavian Cardiac Outcome Trial) substudy. *Journal of the American College of Cardiology* 56: 24-30, 2010.
47. **Mynard JP, and Smolich JJ**. Wave potential and the one-dimensional windkessel as a wave-based paradigm of diastolic arterial hemodynamics. *American Journal of Physiology-Heart and Circulatory Physiology* 307: H307-H318, 2014.
48. **Long JS, and Ervin LH**. Using heteroscedasticity consistent standard errors in the linear regression model. *The American Statistician* 54: 217-224, 2000.
49. **Aghilinejad A, Wei H, and Pahlevan NM**. Non-Invasive Pressure-Only Aortic Wave Intensity Evaluation Using Hybrid Fourier Decomposition-Machine Learning Approach. *IEEE Transactions on Biomedical Engineering* 2023.
50. **Alavi R, Aghilinejad A, Wei H, Niroumandi S, Wieman S, and Pahlevan NM**. A coupled atrioventricular-aortic setup for in-vitro hemodynamic study of the systemic circulation: Design, fabrication, and physiological relevancy. *Plos one* 17: e0267765, 2022.
51. **Pahlevan NM, and Gharib M**. A wave dynamics criterion for optimization of mammalian cardiovascular system. *Journal of biomechanics* 47: 1727-1732, 2014.

52. **Khan H, Kalogeropoulos AP, Georgiopoulou VV, Newman AB, Harris TB, Rodondi N, Bauer DC, Kritchevsky SB, and Butler J**. Frailty and risk for heart failure in older adults: the health, aging, and body composition study. *Am Heart J* 166: 887-894, 2013.
53. **Brubaker PH, and Kitzman DW**. Chronotropic incompetence: causes, consequences, and management. *Circulation* 123: 1010-1020, 2011.
54. **Namasivayam M, McDonnell BJ, McEniery CM, O'Rourke MF, and Anglo-Cardiff Collaborative Trial Study I**. Does wave reflection dominate age-related change in aortic blood pressure across the human life span? *Hypertension* 53: 979-985, 2009.
55. **Hughes D, Judge C, Murphy R, Loughlin E, Costello M, Whiteley W, Bosch J, O'Donnell MJ, and Canavan M**. Association of blood pressure lowering with incident dementia or cognitive impairment: a systematic review and meta-analysis. *Jama* 323: 1934-1944, 2020.
56. **Goel A, Maroules CD, Mitchell GF, Peshock R, Ayers C, McColl R, Vongpatanasin W, and King KS**. Ethnic Difference in Proximal Aortic Stiffness: An Observation From the Dallas Heart Study. *JACC Cardiovascular imaging* 10: 54-61, 2017.
57. **Kozakova M, Morizzo C, Guarino D, Federico G, Miccoli M, Giannattasio C, and Palombo C**. The impact of age and risk factors on carotid and carotid-femoral pulse wave velocity. *Journal of hypertension* 33: 1446-1451, 2015.
58. **Jefferson AL, Cambronero FE, Liu D, Moore EE, Neal JE, Terry JG, Nair S, Pechman KR, Rane S, and Davis LT**. Higher aortic stiffness is related to lower cerebral blood flow and preserved cerebrovascular reactivity in older adults. *Circulation* 138: 1951-1962, 2018.
59. **Aghilinejad A, Amlani F, Liu J, and Pahlevan NM**. Accuracy and applicability of non-invasive evaluation of aortic wave intensity using only pressure waveforms in humans. *Physiological Measurement* 42: 105003, 2021.
60. **Kang J, Aghilinejad A, and Pahlevan NM**. On the accuracy of displacement-based wave intensity analysis: Effect of vessel wall viscoelasticity and nonlinearity. *PloS one* 14: e0224390, 2019.
61. **Hughes AD, Park C, Ramakrishnan A, Mayet J, Chaturvedi N, and Parker KH**. Feasibility of estimation of aortic wave intensity using non-invasive pressure recordings in the absence of flow velocity in man. *Frontiers in physiology* 11: 550, 2020.
62. **Chiesa ST, Masi S, Shipley MJ, Ellins EA, Fraser AG, Hughes AD, Patel RS, Khir AW, Halcox JP, and Singh-Manoux A**. Carotid artery wave intensity in mid-to late-life predicts cognitive decline: the Whitehall II study. *European heart journal* 40: 2300-2309, 2019.
63. **Aghilinejad A, Alavi R, Rogers B, Amlani F, and Pahlevan NM**. Effects of vessel wall mechanics on non-invasive evaluation of cardiovascular intrinsic frequencies. *Journal of Biomechanics* 129: 110852, 2021.
64. **López-Vázquez JC, Deán-Ben XL, Trillo C, Doval ÁF, Fernandez JL, Amlani F, and Bruno OP**. Numerical modeling and measurement by pulsed television holography of ultrasonic displacement maps in plates with through-thickness defects. *Optical Engineering* 49: 095802-095802-095810, 2010.
65. **Bilgi C, Amlani F, Wei H, Rizzi N, and Pahlevan NM**. Thermal and Postural Effects on Fluid Mixing and Irrigation Patterns for Intraventricular Hemorrhage Treatment. *Annals of Biomedical Engineering* 1-14, 2023.
66. **Mynard J, and Nithiarasu P**. A 1D arterial blood flow model incorporating ventricular pressure, aortic valve and regional coronary flow using the locally conservative Galerkin (LCG) method. *Communications in numerical methods in engineering* 24: 367-417, 2008.

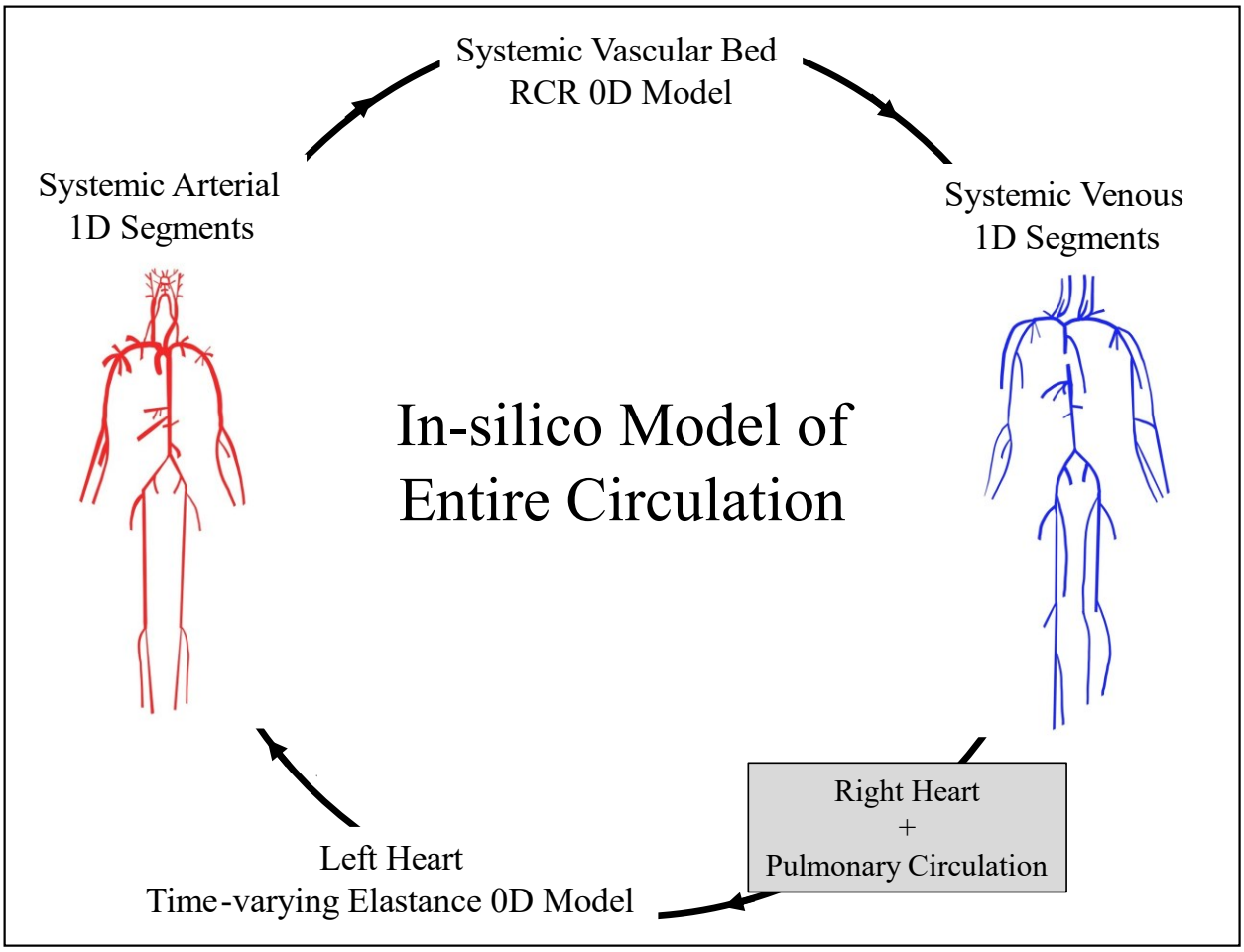

Figure 11 Closed-loop cardiovascular model consisting of 1D segments coupled to 0D lumped-parameter models of the heart and microvasculature.

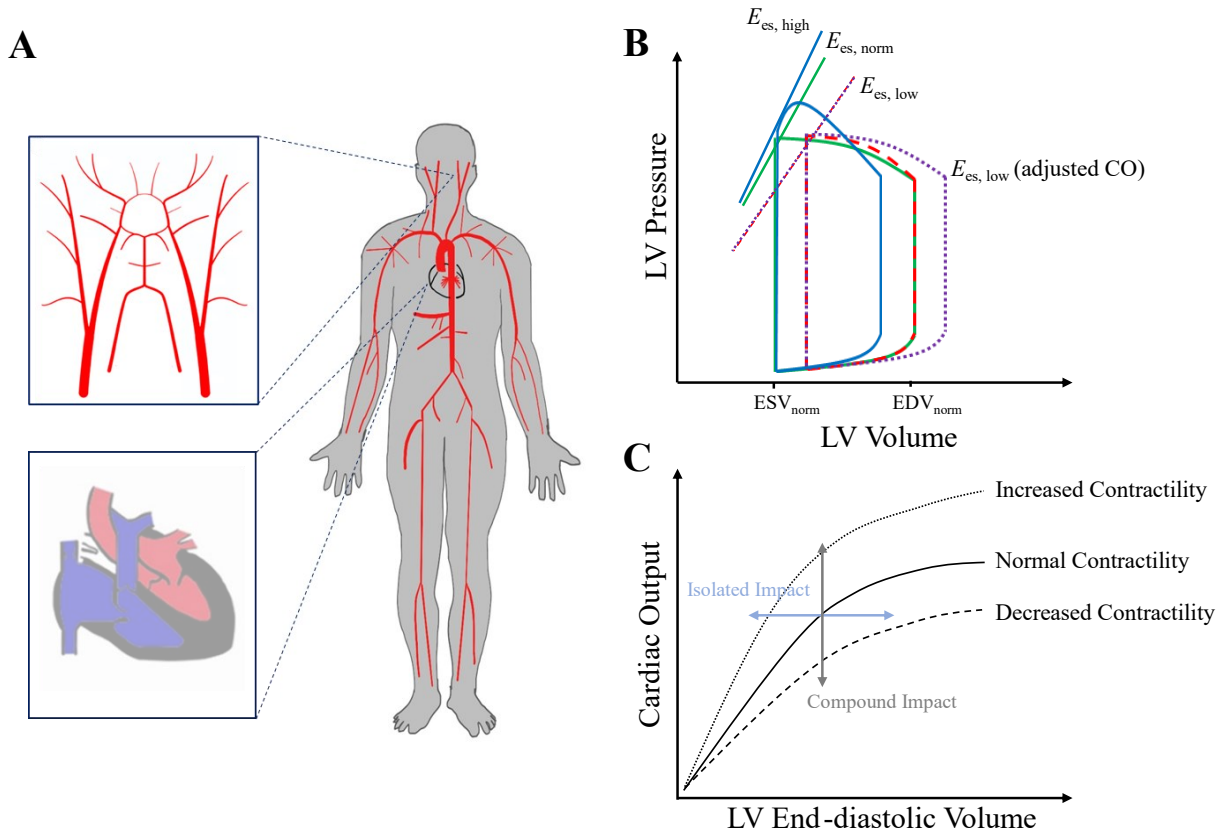

Figure 12 A: schematic representation of the human circulatory system. B: interventricular pressure-volume loops for different cases of contractility (demarcated in different line styles and colors). ESV and EDV, end-systolic volume and end-diastolic volume, respectively. C: compounded impact [a fixed left ventricular end-diastolic volume (LVEDV)] and the isolated impact [a fixed cardiac output (CO)] of contractility. Ees, end-systolic elastance.

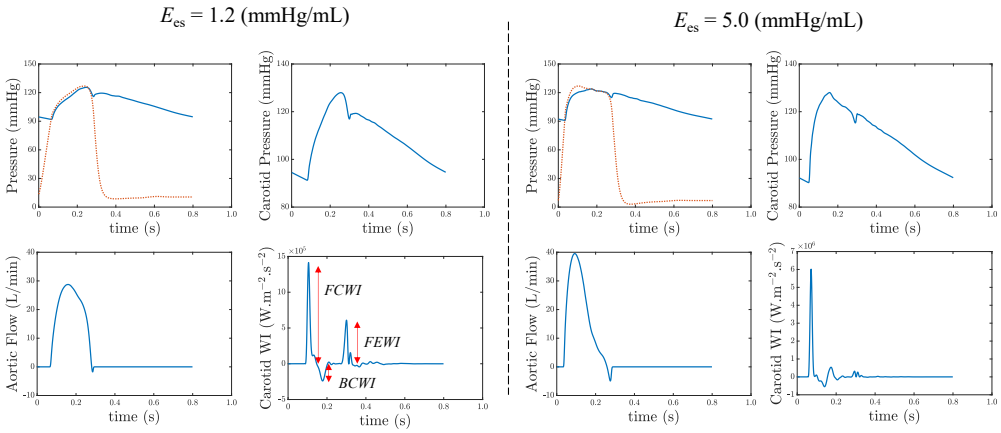

Figure 13 Effects of LV contractility on *aortic and carotid* hemodynamics. *CO* is the same for both sets of figures on the right and left panels. The figures on the left panel demonstrate the impact of reduced contractility, and the figures on the right panel demonstrate the impact of increased contractility. FCWI: Forward Compression Wave Intensity; BCWI: Backward Compression Wave Intensity; FEWI: Forward Expansion Wave Intensity.

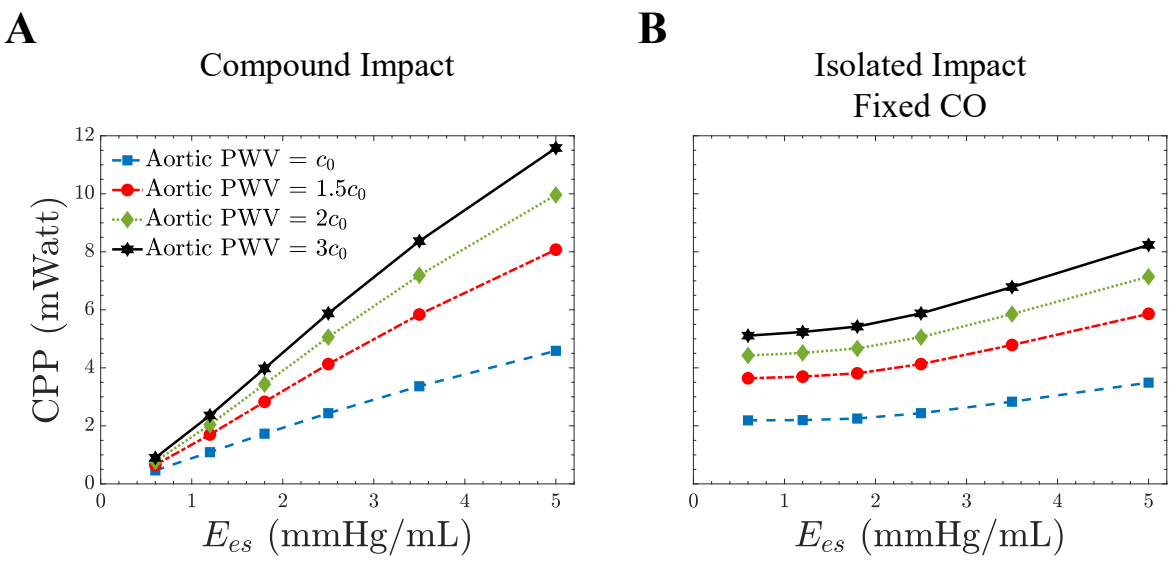

Figure 14 Carotid pulsatile power (CPP) per cardiac cycle vs. contractility [as measured by end-systolic elastance (Ees)] at different levels of aortic stiffness at fixed left ventricular end-diastolic volume [LVEDV, changing cardiac output (CO); A] and fixed CO (B).

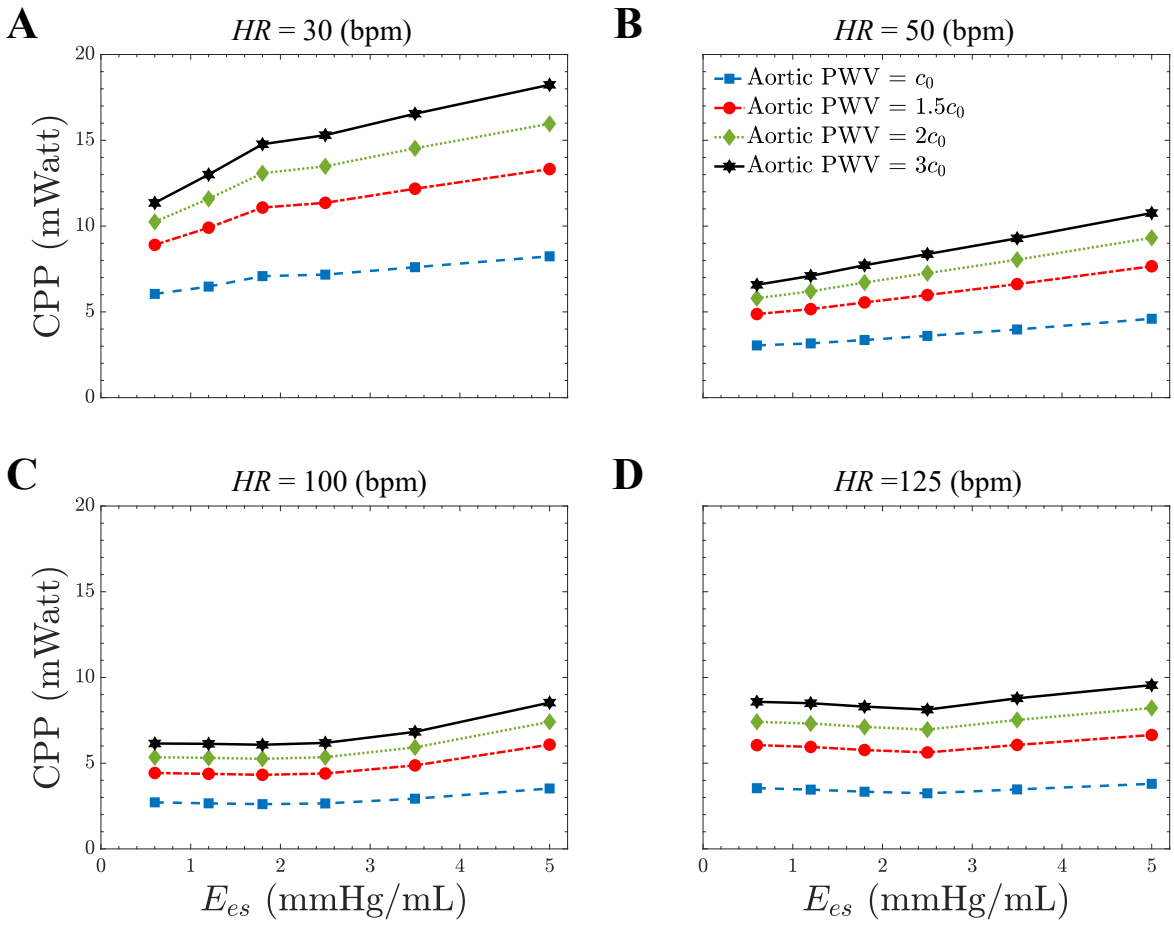

Figure 15 Carotid pulsatile power (CPP) per cardiac cycle vs. contractility [as measured by end-systolic elastance (Ees)] at different levels of aortic stiffness at other heart rates (HR; in beats/min): 30 (A), 50 (B), 100 (C), and 125 (D).

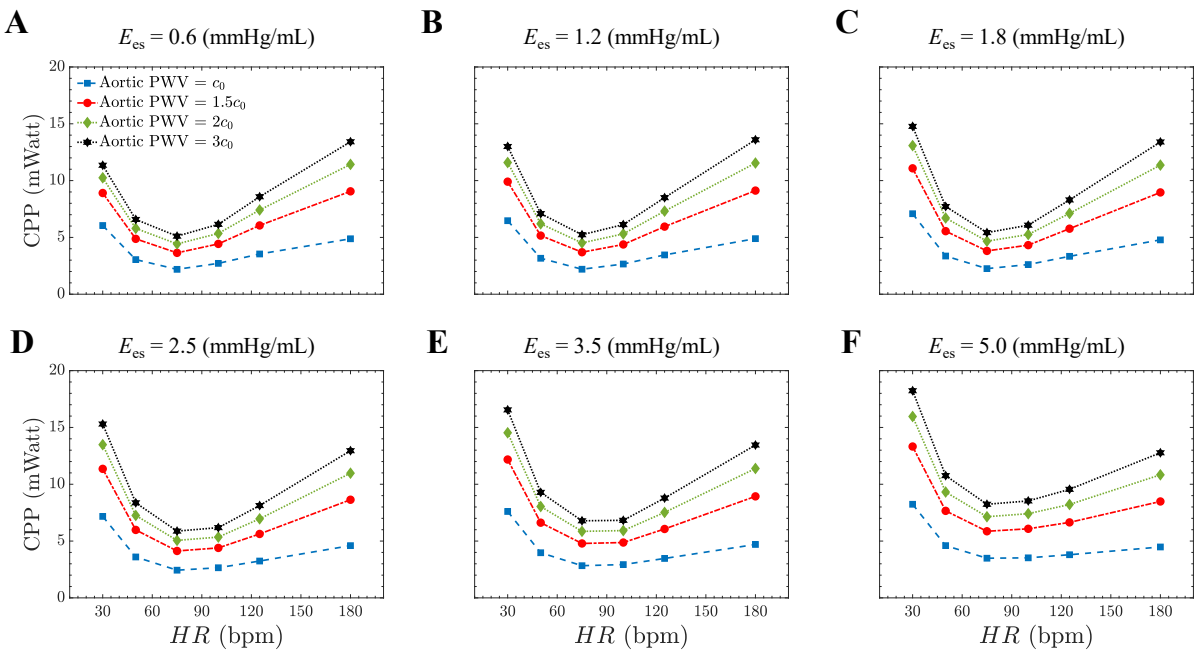

Figure 16 Carotid pulsatile power (CPP) per cardiac cycle vs. heart rate (HR) at different levels of aortic stiffness: end-systolic elastance (Ees; in mmHg/mL), 0.6 (A), 1.2 (B), 1.8 (C), 2.5 (D), 3.5 (E), and 5.0 (F).

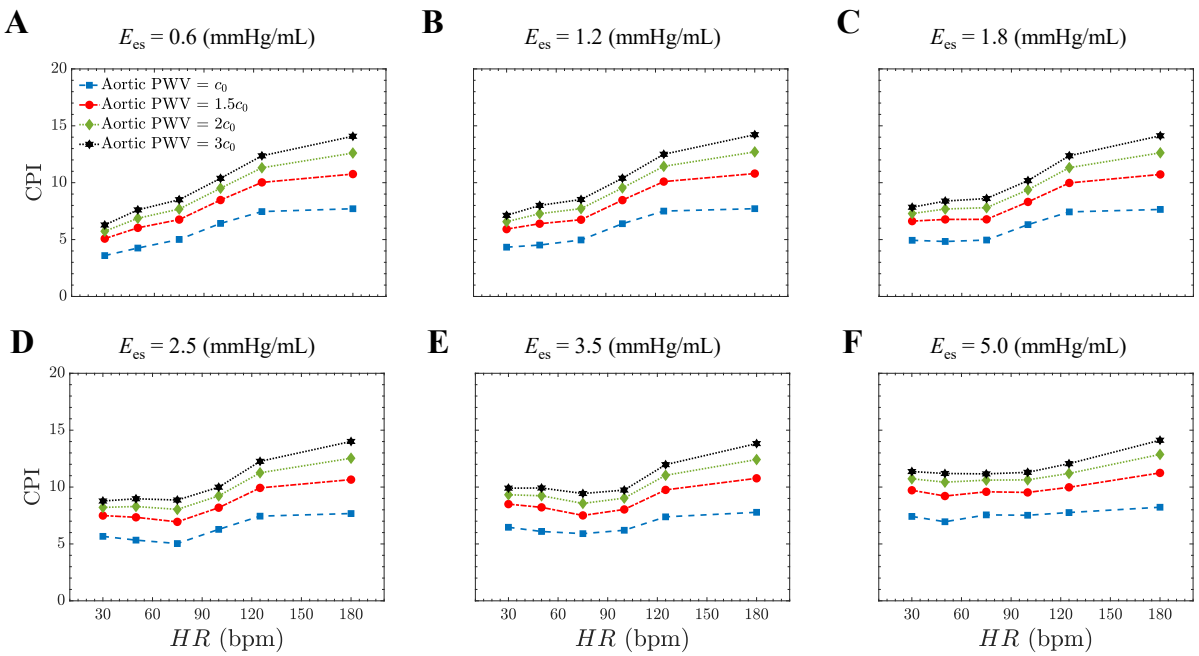

Figure 17 Carotid pulsatility index (CPI) per cardiac cycle vs. heart rate (HR) at different levels of aortic stiffness: end-systolic elastance (Ees; in mmHg/mL), 0.6 (A), 1.2 (B), 1.8 (C), 2.5 (D), 3.5 (E), and 5.0 (F).

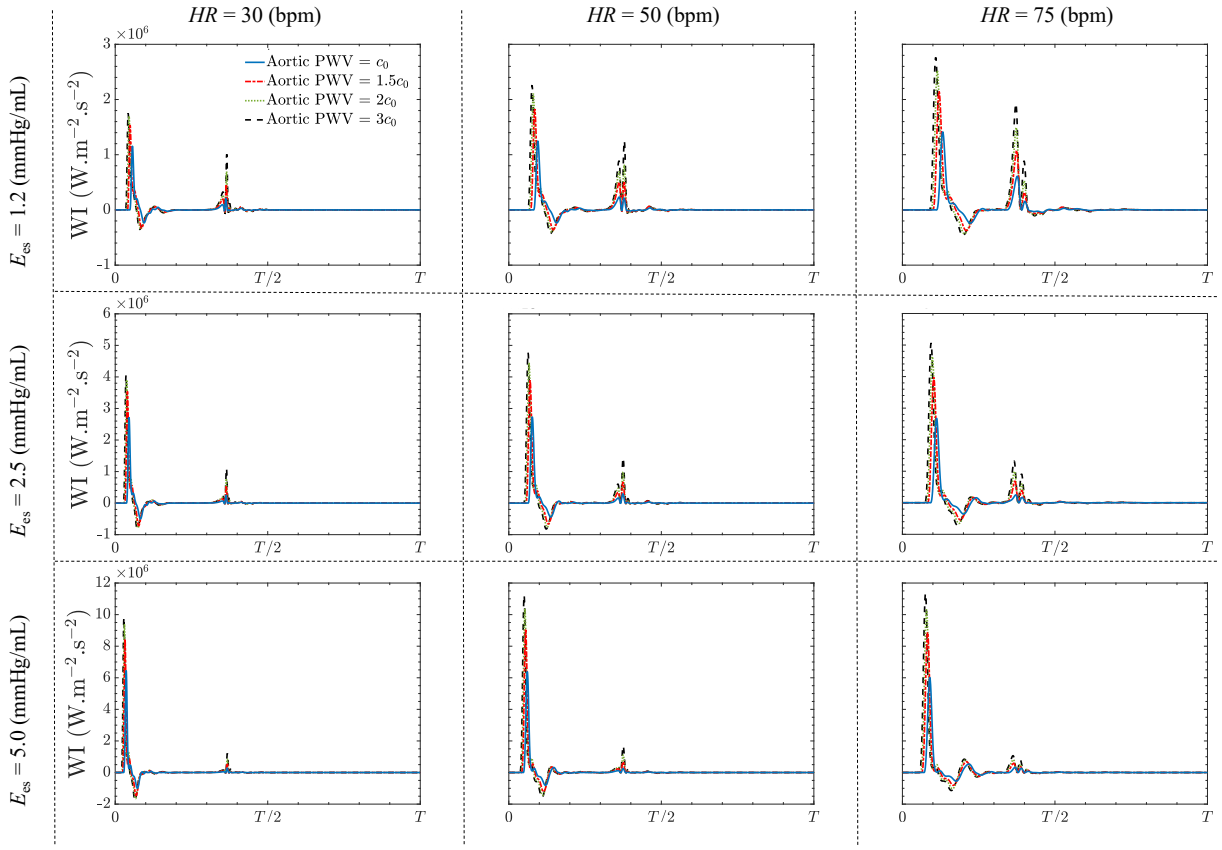

Figure 18 Sample carotid wave intensity (WI) patterns at different heart rate (HR) and different levels of contractility [as measured by end-systolic elastance (Ees)]. Each plot contains data obtained at different levels of aortic stiffness [quantified by pulse wave velocity (PWV)].

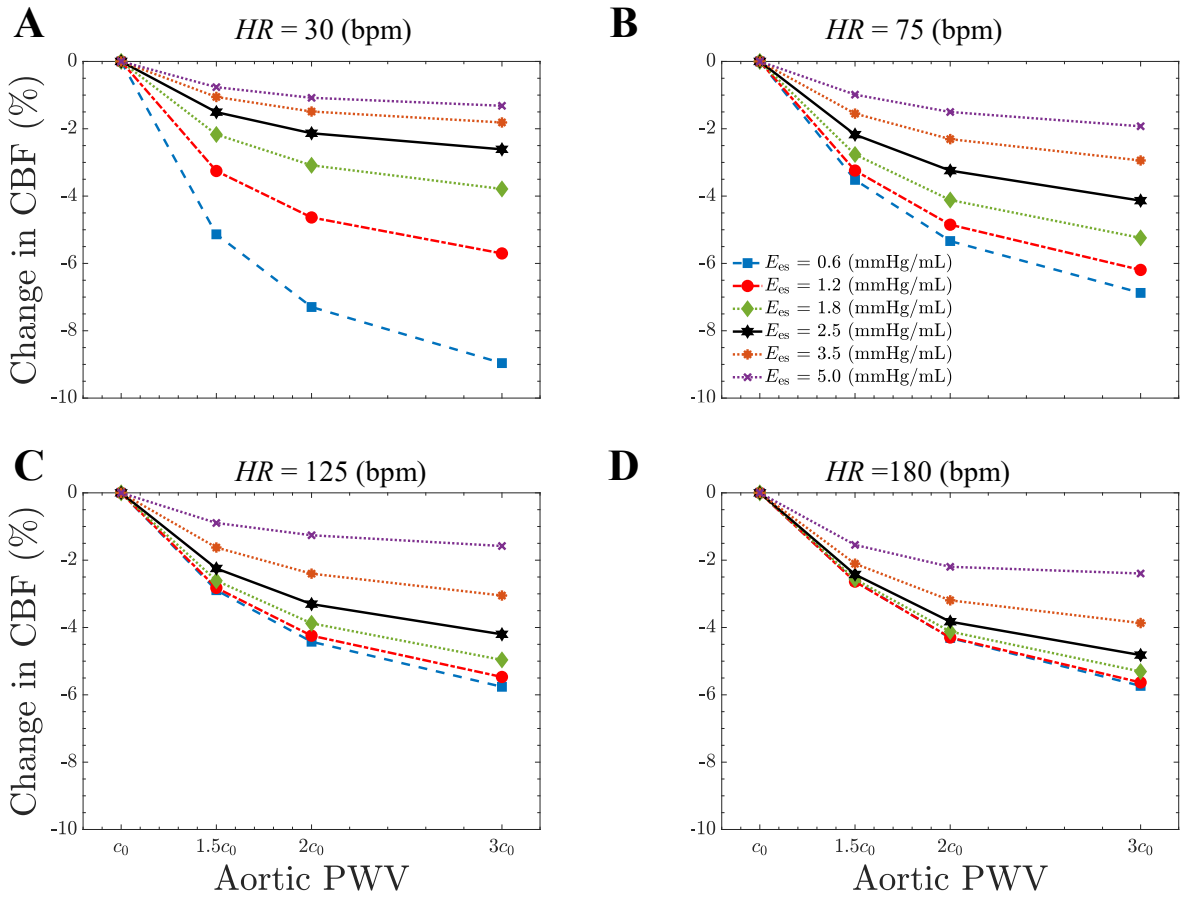

Figure 19 Change in the transmitted flow to the brain vs. aortic stiffness [as measured by pulse wave velocity (PWV)] at different levels of contractility: heart rate (HR; in beats/min), 30 (A), 75 (B), 125 (C), and 180 (D). CBF, cerebral blood flow; Ees, end-systolic elastance.

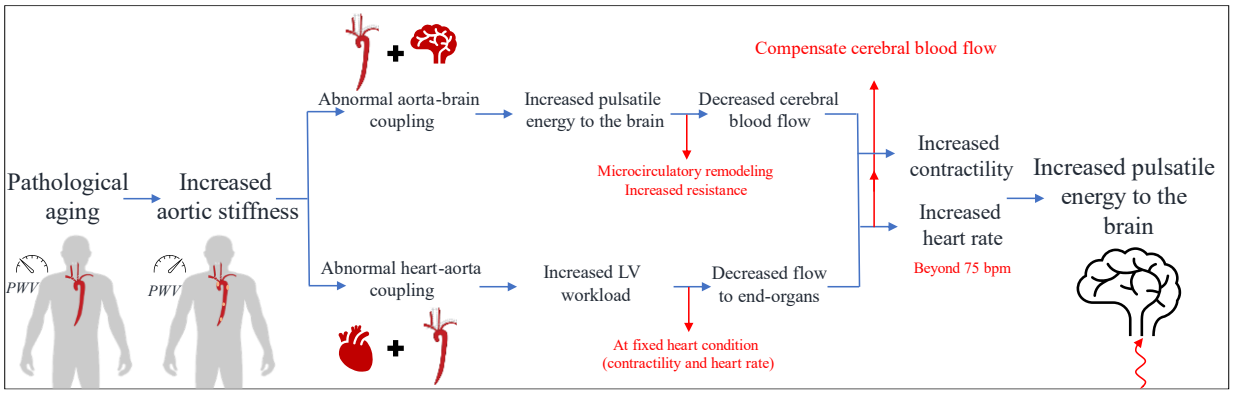

Figure 20 Mechanistic model, based on the findings of this study, for compensating cerebral blood flow due to pathological aging. LV, left ventricular; PWV, pulse wave velocity..

Table 1. Physical parameters used in this study.

Physical Parameter	Unit	Baseline	Range
Aortic PWV	m/s	4.66	[4.66, 13.98]
Heart Rate	bpm	75	[30, 180]
LV End-systolic Elastance	mmHg/mL	2.5	[0.6, 5.0]
LV End-diastolic Volume	mL	136	[65, 465]
Ejection Fraction	%	55	[14, 70]
Stroke Volume	mL	74	[19, 186]
Cardiac Output	L/min	5.56	[1.4, 7.1]

Table 2. Impact of LV contractility at two levels of aortic stiffness on the transmitted pulsatility to the brain.

Contractility (mmHg/ml)	**0.6**	**1.2**	**1.8**	**2.5**	**3.5**	**5.0**
Baseline aortic PWV, c_0						
Carotid Pulsatile Power, CPP (mWatt)	2.19	2.20	2.25	2.44	2.83	3.49
Carotid Pulsatility Index, CPI	5.00	4.96	4.96	5.04	5.90	7.55
Increased aortic PWV, $3c_0$						
Carotid Pulsatile Power, CPP (mWatt)	5.11	5.24	5.42	5.88	6.78	8.24
Carotid Pulsatility Index, CPI	8.50	8.52	8.61	8.86	9.43	11.16

* All values are reported at a heart rate of 75 bpm.

Table 3. Impact of LV contractility on carotid WI indices at different aortic stiffness (PWV).

Contractility (mmHg/mL)	**0.6**	**1.2**	**1.8**	**2.5**	**3.5**	**5.0**
Baseline PWV c_0						
FCWI (W.$m^{-2}.s^{-2}\times10^5$)	9.5	14.2	19.4	26.7	39.0	60.2
BCWI (W.$m^{-2}.s^{-2}\times10^5$)	1.7	2.4	2.9	3.6	4.4	5.2
FEWI (W.$m^{-2}.s^{-2}\times10^5$)	8.8	6.1	3.8	2.5	2.9	5.5
Increased PWV $3c_0$						
FCWI (W.$m^{-2}.s^{-2}\times10^5$)	18.7	27.6	37.1	50.7	74.0	113.0
BCWI (W.$m^{-2}.s^{-2}\times10^5$)	3.4	4..6	5.8	7.1	8.9	11.4
FEWI (W.$m^{-2}.s^{-2}\times10^5$)	8.9	19.0	15.6	13.1	11.6	10.6

* All values are reported at a heart rate of 75 bpm. The effect of contractility is isolated at fixed CO.

Table 4. Impact of heart rate on carotid WI indices at different aortic stiffness (PWV).

Heart Rate (bpm)	**30**	**50**	**75**	**100**	**125**
Baseline PWV c_0					
FCWI (W.$m^{-2}.s^{-2}$)	27.1	27.3	26.7	28.3	28.9
BCWI (W.$m^{-2}.s^{-2}$)	4.9	4.4	3.5	3.1	2.5
FEWI (W.$m^{-2}.s^{-2}$)	2.5	2.9	2.5	6.8	19.9
Increased PWV $3c_0$					
FCWI (W.$m^{-2}.s^{-2}$)	40.4	47.7	50.7	55.2	58.2
BCWI (W.$m^{-2}.s^{-2}$)	8.1	8.2	7.1	6.4	5.5
FEWI (W.$m^{-2}.s^{-2}$)	10.9	14.3	13.2	18.6	46.3

* All values are reported at a contractility of 2.5 mmHg/mL.

APPENDIX

The numerical model

The numerical methodology for solving the partial differential equation (PDE) system of Eqs. (1)-(2) is based on a Fourier continuation (FC) approach that has been introduced previously for 1D arterial wave propagation [JCP 2020]. Both implicit and explicit FC-based PDE solvers have been successfully constructed and utilized for a variety of physical problems, including those governed by advection-diffusion equations**,** Navier-Cauchy elastodynamics equations, Navier-Stokes fluid equations, and fluid-structure equations [27, 28, 34, 56, 57].

Validations of the complete numerical solver have been conducted using the benchmark problems proposed in [33]. Fig. A1 presents pressure and flow solutions of a single-segment common carotid artery (with Windkessel) benchmark using both FC as well as commonly used discontinuous Galerkin (DCG) [33] and locally conservative Galerkin (LCG) methods [58]. Figs. A2 additionally presents corresponding FC, DCG and LCG simulated pressure and flow at midpoints of various vascular segments from a benchmark problem [33] on a 77-segment open-loop model (that considers 56 major arteries). Parameters for these benchmarks can be found in the respective source [33]. For both problems, Figs. A1 and A2 demonstrate excellent correspondence between the solutions generated by the FC solver employed in this work and those generated by other numerical schemes.

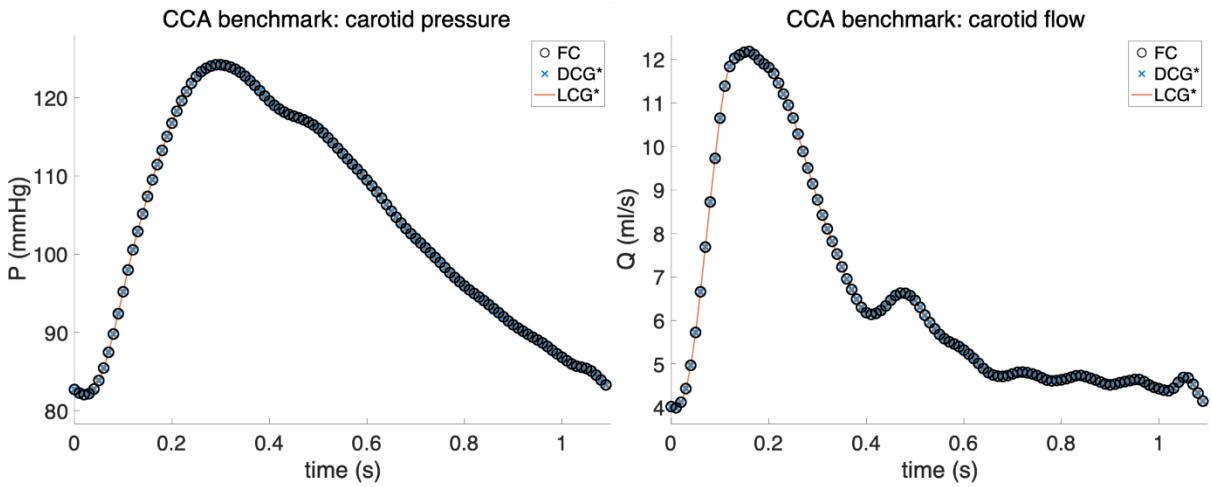

Figure A1 Single segment benchmark. Pressure (left) and flow rate (right) at the midpoint of the common carotid artery (CCA) simulated by Fourier continuation (FC; the solver used in this work), discontinuous Galerkin (DCG) [33], and locally conservative Galerkin (LCG) [58] methods. Lines are plotted at a resolution of $\Delta t = 10^{-3}s$, and markers are plotted every 10 such timesteps ($10^{-2}\ s$) for easier visualization. *Provided by the supplementary data files in [33].

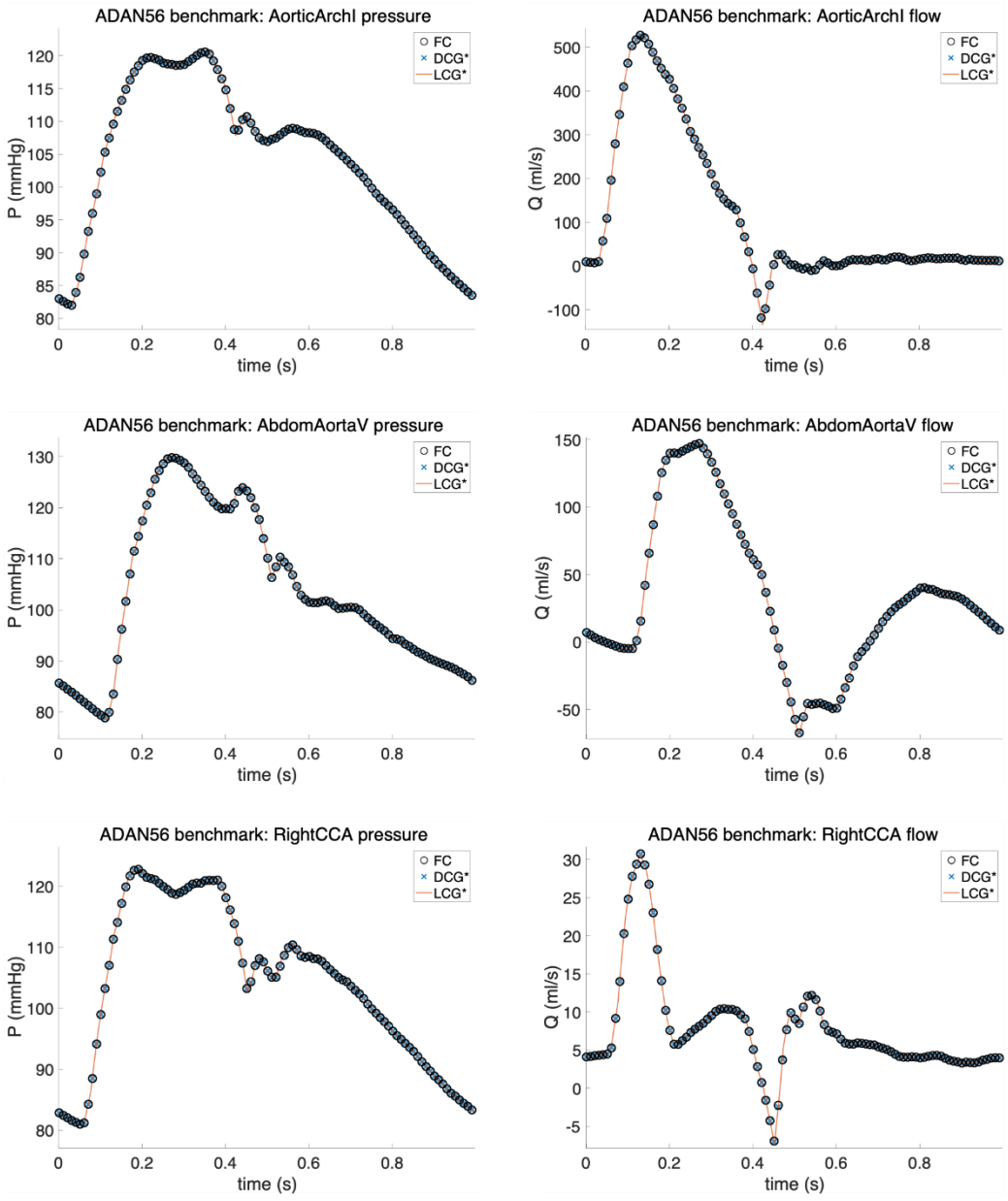

Figure A2 77-segment (ADAN56) benchmark. Pressure (left) and flow rate (right) at the midpoint of (from top row to bottom) the aortic arch (AorticArchI), abdominal aorta (AbdomAortaV), and right common carotid artery (RightCCA) simulated by Fourier continuation (FC), discontinuous Galerkin (DCG) [33], and locally conservative Galerkin (LCG) [58] methods. Lines are plotted at a resolution of $\Delta t = 10^{-3}s$, and markers are plotted every 10 such timesteps ($10^{-2}\ s$) for easier visualization. *Provided by the supplementary data files in [33].

Statistical analysis

The summary of the Shapiro-Wilk test to check the normality of each regression's residuals is presented in Table A1.

Table A1. Summary of Shapiro-Wilk test to check normality.

Model	p-value
Model With CPI as the dependent variable	0.471
Model with CPP as the dependent variable	0.957
Model with CBF as the dependent variable	0.979

The regression model outcomes for three dependent variables, CPI, CPP, and CBF, are presented in Tables A2, A3, and A4, respectively. Independent variables in this study are LV contractility, aortic PWV, and heart rate. All independent variables are incorporated in the models as categorical variables. The minimum baseline for the heart rate is 30 bpm, for the contractility is 0.6 mmHg/mL, and for the aortic PWV is c_0.

Table A2. Summary of regression statistics for CPI as a dependent variable.

Variable	Estimate	Robust standard error (HC3)	t-statistics	p-value
Intercept	4.176	0.332	12.563	<0.001
Heart Rate 50 bpm	0.205	0.267	0.7673	0.444
Heart Rate 75 bpm	0.348	0.257	1.353	0.178
Heart Rate 100 bpm	1.438	0.262	5.497	<0.001
Heart Rate 125 bpm	2.954	0.289	10.210	<0.001
Heart Rate 180 bpm	4.039	0.321	12.581	<0.001
Contractility 1.2 mmHg/mL	0.223	0.262	0.851	0.397
Contractility 1.8 mmHg/mL	0.350	0.238	1.469	0.144
Contractility 2.5 mmHg/mL	0.578	0.232	2.494	0.013
Contractility 3.5 mmHg/mL	0.936	0.262	3.570	<0.001
Contractility 5.0 mmHg/mL	1.992	0.304	6.549	<0.001
PWV 1.5 c_0	2.184	0.180	12.150	<0.001
PWV 2.0 c_0	3.333	0.190	17.554	<0.001
PWV 3.0 c_0	4.211	0.210	20.073	<0.001

Table A3. Summary of regression statistics for CPP as a dependent variable.

Variable	Estimate	Robust standard error (HC3)	t-statistics	p-value
Intercept	7.642	0.4383	17.436	<0.001
Heart Rate 50 bpm	-5.2815	0.3392	-15.569	<0.001
Heart Rate 75 bpm	-6.9915	0.3628	-19.273	<0.001
Heart Rate 100 bpm	-6.5587	0.3538	-18.537	<0.001
Heart Rate 125 bpm	-5.172	0.332	-15.584	<0.001
Heart Rate 180 bpm	-2.034	0.4437	-4.584	<0.001
Contractility 1.2 mmHg/mL	0.2442	0.334	0.731	0.446
Contractility 1.8 mmHg/mL	0.483	0.320	1.51	0.133
Contractility 2.5 mmHg/mL	0.604	0.316	1.909	0.058
Contractility 3.5 mmHg/mL	1.195	0.330	3.625	<0.001
Contractility 5.0 mmHg/mL	1.9974	0.3776	5.289	<0.001
PWV 1.5 c_0	2.785	0.241	11.547	<0.001
PWV 2.0 c_0	4.292	0.263	16.319	<0.001
PWV 3.0 c_0	5.582	0.309	18.042	<0.001

Table A4. Summary of regression statistics for CBF as a dependent variable.

Variable	Estimate	Robust standard error (HC3)	t-statistics	p-value
Intercept	0.709	0.005	149.144	<0.001
Heart Rate 100 bpm	0.003	0.003	0.936	0.352
Heart Rate 125 bpm	0.016	0.004	3.921	<0.001
Heart Rate 180 bpm	0.008	0.003	2.434	0.017
Contractility 1.2 mmHg/mL	0.006	0.003	1.879	0.064
Contractility 1.8 mmHg/mL	0.013	0.004	3.394	0.001
Contractility 2.5 mmHg/mL	0.012	0.003	3.646	<0.001
Contractility 3.5 mmHg/mL	0.032	0.004	7.757	<0.001
Contractility 5.0 mmHg/mL	0.0288	0.004	6.541	<0.001
PWV 1.5 c_0	-0.017	0.003	-5.316	<0.001
PWV 2.0 c_0	-0.025	0.003	-7.739	<0.001
PWV 3.0 c_0	-0.032	0.003	-9.144	<0.001